

# Elucidating loessal landslide initiation in wood- and shrub-land by hydro-mechanical heterogeneity

Ruijie Yang, Chao Ma, Xi Yang, Yan Zhang, Liqun Lyu, Xinying Wang

School of Soil and Water Conservation, Beijing Forestry University, Beijing 100083, PR China

Corresponding author: Professor Chao Ma, sanguoxumei@163.com

**Abstract:** Vegetation recovery on the Chinese Loess Plateau has markedly changed the hydrological and mechanical controls on hillslope erosion, shifting sediment production from runoff-driven erosion to gravity-driven processes such as rainfall-induced loessal landslides. Presently, few studies have clearly documented the differences in landslide erosion and initiation between shrubland and woodland. We conducted field investigations, rainfall soil-moisture observations, dye-tracer experiments, and soil-root tests, to examine landslide characteristics in terms of geometry and volume, excess soil-water ratio, preferential-flow pathways, and failure potential in the two stands. Rainfall-induced loessal landslides in the shrubland stand have shallower failure depths and smaller volumes but are wider than those in the woodland stand, and they are triggered under lower contributing area-slope conditions. Moreover, vertical infiltration in the woodland stand tends to be more stable and efficient, characterized by greater water penetration depth and enhanced pore connectivity. The relationship between the excess soil-water ratio and soil-water storage demonstrates that subsurface flow in woodland stand is triggered at relatively lower degrees of saturation. This behavior is attributed to well-developed preferential-flow pathways and reduced matric suction. The landscape dissection-rainfall index indicates lower landslide susceptibility on steep woodland slopes than on steep shrubland slopes, consistent with the lower landslide density in woodland relative to shrubland. Overall, these hydrological and mechanical contrasts indicate that woodland slopes, by combining deep root systems, stable preferential-flow pathways, and strong mechanical reinforcement, support an effective subsurface flow system that enhances infiltration and delays shallow saturation, thus improving slope stability. These results highlight the need to reassess sediment production on the Loess Plateau by explicitly accounting for landslides rather than attributing it solely to runoff-driven erosion.

**Keywords:** Shallow landslide; Hillslope hydrology; Landscape dissection-rainfall index

## 1 Introduction

The Chinese Loess Plateau is one of the most erosive landscapes in the world (Fu et al., 2016; Borrelli et al., 2020; Bai et al., 2024). Since 1980, ecological rehabilitation has significantly improved regional vegetation cover and structure, with vegetation cover now reaching approximately 60% (Feng et al., 2016; Deng et al., 2022; Liao et al., 2025). Restored vegetation, optimized plant community structure, and surface litter accumulation have enhanced water storage capacity and slope stability (Yan et al., 2024; Liu et al., 2025). Since 2010, the region has experienced several rainstorms that are unprecedented in the historical record, as exemplified by storms in 2013, 2017, and 2025 (Tang et al., 2020; Deng et al., 2022; Yang et al., 2023; Hao et al., 2024). Subsequent studies have reported a shift in the dominant erosion process from dispersed runoff erosion to gravitational mass movements (Yang et al., 2024; Du et al., 2025). These findings sufficiently indicate that vegetation recovery on Chinese Loess Plateau alters the dominant sediment-producing processes and soil-erosion patterns.

Vegetation recovery can enhance ecosystem functioning and alter the rainwater infiltration pathways (Gu et al., 2019; Wang et al., 2022; Guan et al., 2024). Increases in surface cover and root penetration significantly enhance rainfall infiltration and promote greater spatial heterogeneity, non-uniform infiltration patterns, and preferential-flow pathways (Li et al., 2007; Zhao et al., 2022). Preferential flow often serves as a primary pathway for rainfall infiltration and can bypass soil-matrix pores to reach deeper soil layers (Bachmair et al., 2012; Franklin et al., 2021).

42 Preferential flow intensity and morphology vary markedly among vegetation types. Woodland slopes are  
43 characterized by deep, continuous macropore channels, predominantly vertical preferential flow, rapid infiltration,  
44 and greater deep-soil water storage (Niu et al., 2023; Cai et al., 2024; Zhang et al., 2025). Shrubland slopes exhibit  
45 predominantly lateral and diffuse subsurface flow with weak vertical components, thereby retaining much of the  
46 infiltrating water in shallow soil layers (Wang et al., 2020; An et al., 2022; Liang et al., 2023; Zhang et al., 2024).  
47 Herbaceous slopes rely mainly on surface cracks and earthworm burrows to route water, and therefore preferential  
48 flow channels are sparse and discontinuous (Wen et al., 2020; Niu et al., 2023; Li et al., 2025). Vegetation recovery  
49 has significantly restructured the soil bio-pore system through root penetration, thereby facilitating the development  
50 of preferential-flow pathways and making infiltration regimes more heterogeneous (Zhao et al., 2022; Guan et al.,  
51 2024). However, preferential-flow infiltration on steep slopes, particularly at landslide sites with different vegetation  
52 types, has not been adequately investigated. During heavy storms, preferential flow can regulate spatiotemporal  
53 subsurface water dynamics and act as a biologically mediated control on slope stability.

54 Root morphology and spatial configuration influence rainwater infiltration pathways and soil-moisture  
55 redistribution (Fan et al., 2020; Li et al., 2023). On the Chinese Loess Plateau, two predominant vegetation types are  
56 recognized: woodlands dominated by *Robinia pseudoacacia* and *Pinus tabulaeformis*, and shrublands dominated by  
57 *Rosa xanthina* and *Hippophae rhamnoides*. Woodland trees typically develop deeply penetrating root systems,  
58 forming continuous macropore networks and vertical preferential-flow pathways (Zhao et al., 2022; Cai et al., 2024;  
59 Wang and Zhang, 2024). These structures facilitate rapid rainfall infiltration into deep soil layers, enhance subsurface  
60 moisture retention, delay surface saturation, and reduce surface runoff (Souza et al., 2023; Cai et al., 2024; Hu et al.,  
61 2025). In contrast, shrubs develop a dense, fibrous root matrix that promotes mesopores and capillaries formation,  
62 thereby accelerating the formation of subsurface saturation zones and limiting vertical percolation (Laycock et al.,  
63 1967; Souza et al., 2023; Xiao et al., 2024; Yamase et al., 2024). Therefore, plant roots can control preferential-flow  
64 patterns and alter hillslope hydrology. However, few studies have examined how the hydrological effects of mature  
65 vegetation influence landslides on the Chinese Loess Plateau.

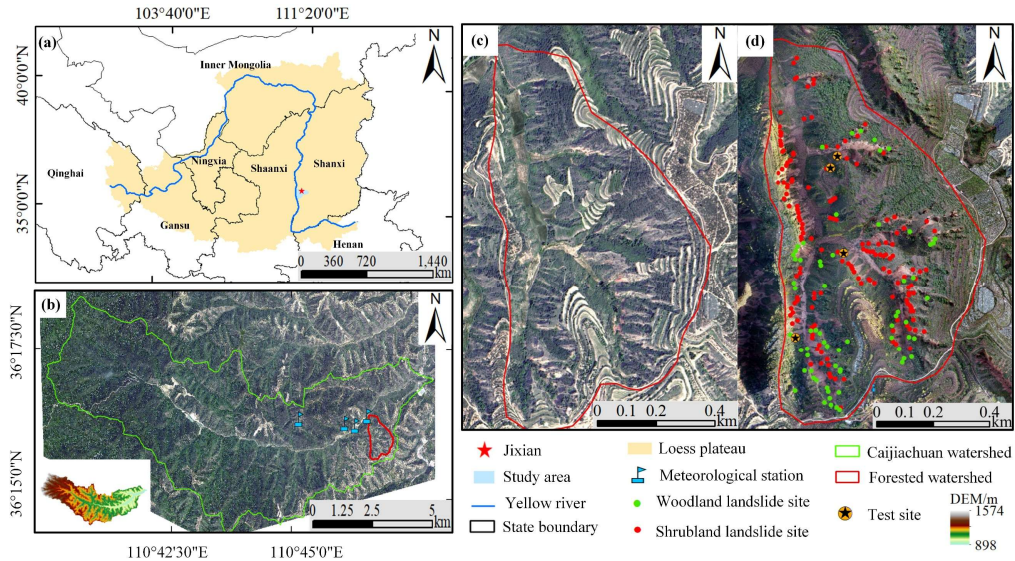
66 To examine the hydrological and mechanical heterogeneity in mature woodland and shrubland stands on steep  
67 slopes and its implications for slope stability, we first analyze landslide geometry and landscape dissection for slides  
68 triggered by a low-intensity storm from 3 to 6 October 2021. Then, we assess hydrological heterogeneity in mature  
69 woodland and shrubland using soil-moisture observations, excess soil-water ratios across different soil-water storage  
70 levels, and preferential-flow pathway identification. Mechanical heterogeneity is characterized by soil and root  
71 strength parameters, the soil water characteristic curve (SWCC), and the hydraulic conductivity function (HCF).  
72 Finally, we evaluate slope failure potential in relation to landslide density in the two stands. This study mainly  
73 addresses the role of vegetation in modulating slope stability by analyzing real landslide cases. Our findings highlight  
74 the dual role of vegetation in mitigating landslide erosion and provide new insights into its nuanced effects on  
75 hillslope stability.

## 76 **2. Research background**

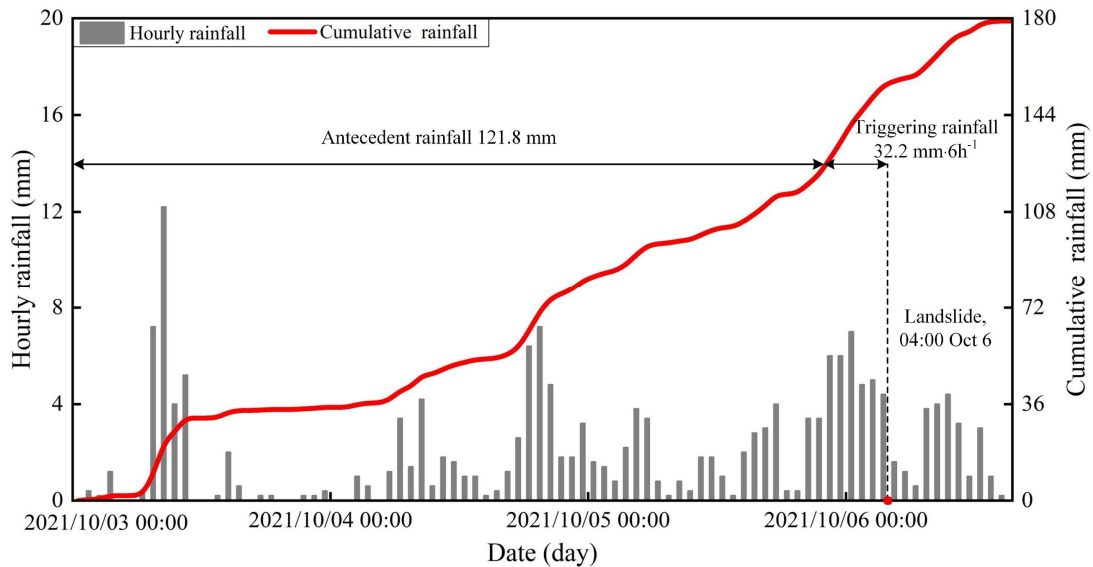
### 77 **2.1 Study area**

78 The study area lies in a forested catchment on the southeastern Loess Plateau in China (Fig. 1a). It is located in  
79 the downstream reach of the Caijiachuan watershed in Jixian County, Shanxi Province (Fig. 1b). The soil has an  
80 unconsolidated, porous structure. On steep slopes, woodland is dominated by *Robinia pseudoacacia* and shrubland  
81 by *Rosa xanthina*. Since the farmland reforestation policy was implemented in 1980, forest cover has recovered to  
82 about 70%. During 1990–1995 and 1999–2002, the Mountain Improvement Technology Training Project enhanced  
83 forest regeneration. Currently, the local soil and water conservation measures serve as a benchmark within the Loess

84 Plateau region. The area has four distinctive seasons and a cold semi-arid climate . The annual precipitation is  
 85 approximately 579.1 mm, and the mean annual temperature is 9.9°C . Most rain events occurs from June to September,  
 86 accounting for more than 70% of the annual precipitation. Prior to the 2021 event, a short-duration storm on 25–26  
 87 August 2003 triggered 18 landslides, with antecedent precipitation of 71.7 mm over 18 hours and an intense 3 h  
 88 rainfall of 24.4 mm (Wang et al., 2024). In contrast, the 2021 rainfall event was a low-intensity storm with prolonged  
 89 antecedent precipitation of 121.8 mm over 72 hours and a 6 h peak rainfall of 32.2 mm (Fig. 2). After the storm,  
 90 post-storm documentation mainly focused on differences in landslide numbers, densities, slope aspects, and  
 91 morphological metrics (Tang et al., 2023), while giving little attention to the hydrological and mechanical conditions  
 92 of landslides in the two forested land types.



93  
 94 **Figure 1.** Geographical setting of the study area, with the (a) location of Caijiachuan watershed in the Loess Plateau,  
 95 China, (b) the forested catchment and meteorological stations in downstream reach of Caijiachuan watershed, (c)  
 96 0.15 m resolution orthoimage on 12 October 2019, and (d) 0.10 m resolution orthoimage on 14 October 2021  
 97 showing the sites for soil-moisture observations and dye-tracer experiments.



98  
 99 **Figure 2.** Hourly and cumulative rainfall from 3 to 6 October 2021.

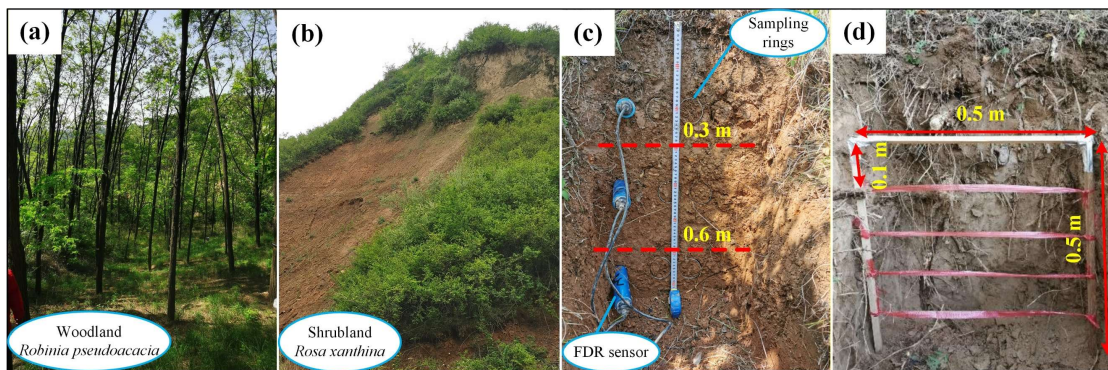
100 **3 Materials and methods**

101 **3.1 Landslide information interpretation**

102 To obtain landslide inventories for the woodland and shrubland, we acquired high-resolution orthoimages and  
103 digital elevation models (DEMs) using an unmanned aerial vehicle (UAV; DJI Inspire 2). Two systematic UAV  
104 flights with consistent flight and image overlap settings were conducted on 12 October 2019 (Fig. 1c) and 14 October  
105 2021 (Fig. 1d). Pix4Dmapper (version 4.6, Pix4D SA, Switzerland) was used to generate ortho-mosaics and DEMs.  
106 These DEMs have spatial resolutions of 0.15 m and 0.10 m, respectively, thereby supporting accurate landslide  
107 mapping. The landslide depths in the woodland and shrubland were measured during field investigations. Landslide  
108 point and areal densities are calculated by dividing the total number of landslides and the total scar area by the  
109 woodland and shrubland areas, respectively. The lateral extent of each landslide is the sum of the sidewall and head  
110 scarp areas. The unit upslope contributing area is the ratio of the total contributing area to the scar width. Slope  
111 gradients and associated unit contributing areas are computed from the DEM generated on 14 October 2021.

112 **3.2 Rainfall, soil-moisture monitoring and sample collection**

113 In the study area, the woodland has an open structure due to sparse-to-moderate tree density and high canopy  
114 height (Fig. 3a), whereas the shrubland has a closed structure because of high density and low canopy height (Fig.  
115 3b). Each study site is dominated by single woody species, with *Robinia pseudoacacia* in the woodland and *Rosa*  
116 *xanthina* in the shrubland. Both land types have a well-developed herbaceous layer. To investigate the hillslope  
117 hydrology, we used frequency-domain reflectometry (FDR) soil-moisture sensors installed at depths of 30, 60, and  
118 90 cm to record volumetric water content from May to August 2023 (Fig. 3c). A meteorological station at  
119 Caijiachuan Forest Station is approximately 2 kilometers to the northwest of the study area. During soil-moisture  
120 sensor installation, we collected undisturbed soil samples near the FDR sensor locations. Bulk density, porosity,  
121 effective cohesion, internal friction angle, and unsaturated hydraulic properties were determined using an electronic  
122 balance, an oven, a GDS triaxial apparatus, and transient release and imbibition tests (Lu and Godt, 2013). Plant  
123 roots were collected to determine depth-dependent root distribution (Fig. 3d), root diameter, root area ratio, and  
124 tensile strength (Nimmo et al., 2009).



125 **Figure 3.** Soil moisture monitoring and soil and root sampling. (a) Open woodland dominated by *Robinia*  
126 *pseudoacacia*. (b) Close-structure shrubland dominated by *Rosa xanthina*. (c) Trench wall showing soil sampling  
127 and FDR sensor installation. (d) In situ root counting and sampling at 0.1 m depth intervals.  
128

129 **3.3 Excessive soil water due to preferential flow**

130 Previous studies of preferential flow on the Loess Plateau have shown that continuous channels in woodland  
131 enhance deep soil water storage, whereas lateral and dispersed channels in shrubland keep water in shallow soil  
132 layers (Wang et al., 2019; An et al., 2022). Therefore, differences in preferential-flow pathways can result in distinct  
133 soil-moisture responses during the same rainfall event. In this study, we first characterized preferential-flow

134 pathways using dye tracer experiments and then examined soil-moisture responses using observed soil-moisture data.

135 Dye tracer experiments were conducted on vegetated slopes near the soil-moisture monitoring sites to examine  
136 the preferential flow pathways (Fig. 1d). The slope angles were  $35.8^\circ$  at the woodland site and  $38.2^\circ$  at the  
137 shrubland site. An electric sprayer was used to spray a  $4 \text{ g}\cdot\text{L}^{-1}$  brilliant blue solution onto a  $100 \text{ cm} \times 100 \text{ cm}$  plot  
138 (Figs. 4a and 4b). After spraying the solution, the plot was immediately covered with a rainproof cloth to minimize  
139 evaporation. After 24 h, a 5 cm-wide margin of soil was removed from the plot edges, and the core area was  
140 excavated to obtain 10 vertical and 5 horizontal profiles. Excavation grids were established at 0.1 m intervals in both  
141 the longitudinal and transverse directions (Figs. 4c and 4d). Profile images were captured with a digital camera at a  
142 fixed distance and in a parallel orientation, and subsequently processed using Adobe Photoshop (version 2021;  
143 Adobe Inc., USA) and Image-Pro Plus (version 6.0; Media Cybernetics, USA). The proportion of flow marked by  
144 the dye is:

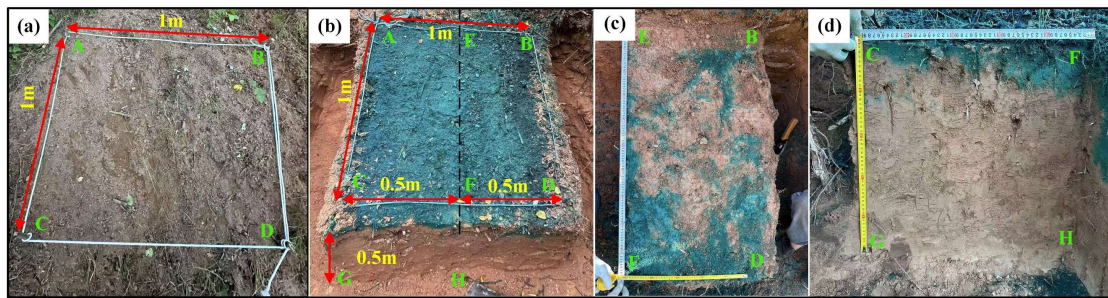
$$145 \quad SAR = \frac{a_j}{A_j} \quad (1)$$

146 where  $SAR$  is the stained-area ratio for the soil profile,  $j$  is soil depth (cm),  $a$  is the number of stained pixels at  
147 depth  $j$ , and  $A$  is the total number of pixels along the image width at depth  $j$ .

148 The soil-moisture response index describes excess soil water in response to a given rainfall input:

$$149 \quad R_C = \frac{R_{max} - (R + R_0)}{R + R_0} \quad (2)$$

150 where  $R_C$  is the excess soil-water ratio in response to a given rainfall event,  $R_{max}$  is the maximum total soil-water  
151 storage during the rainfall episode (mm),  $R$  is the cumulative rainfall during the episode (mm), and  $R_0$  is the initial  
152 total soil-water storage before the rainfall episode (mm). Positive or negative values of  $R_C$  indicate whether the  
153 increase in soil-water storage exceeds or falls below the rainfall input. In addition,  $R_C$  reflects the preferential-flow  
154 component aligned with slope orientation or gravity. As soil moisture typically lags rainfall, we follow the method  
155 proposed by Lu et al. (Lu et al., 2024), which defines rainfall episodes using soil depth and in situ saturated hydraulic  
156 conductivity measurements. Therefore, the  $R_C$  values under different  $R + R_0$  conditions, together with the  
157 preferential-flow pathways, can reflect heterogeneity in soil-water movement in the woodland and shrubland.



158  
159 **Figure 4.** Dye tracer experiments and preferential flow pathways examination. (a) Experimental plot after vegetation  
160 removal. (b) Experimental plot after 24 h of brilliant blue solution spraying. (c) Dye-stained profile parallel to the  
161 slope surface. (d) Dye-stained profile along the gravity direction. Capital letters denote corresponding points shared  
162 across Fig. 4a-d.

### 163 3.4 Slope resistance to failure probability at given rainfall input

164 Hillslope resistance to failure at a given rainfall input depends on the topography and the physical, strength,  
165 and hydraulic properties of soil mass. A widely used combination of the infinite-slope stability model and a  
166 hydrological model yield an expression for the critical drainage area per unit contour length (Montgomery and  
167 Dietrich, 1994):

168 
$$a_{cr} = \frac{zK\sin\theta\cos\theta}{R_t} \left[ \frac{C'+C_r}{\rho_w g z \cos^2 \theta \tan\varphi} + \frac{\rho_s}{\rho_w} \left( 1 - \frac{\tan\theta}{\tan\varphi} \right) \right] \quad (3)$$

169 where  $a_{cr}$  is the critical drainage area per unit contour length ( $\text{m}^2 \cdot \text{m}^{-1}$ ),  $R_t$  is the triggering rainfall rate ( $\text{m} \cdot \text{d}^{-1}$ ),  
 170  $K$  is the saturated hydraulic conductivity ( $\text{m} \cdot \text{d}^{-1}$ ),  $\theta$  is the slope angle ( $^\circ$ ),  $C'$  and  $C_r$  are the effective soil  
 171 cohesion and the root-induced cohesion (kPa),  $\rho_s$  and  $\rho_w$  are the unit weights of soil and water ( $\text{KN} \cdot \text{m}^{-3}$ ),  $z$  is  
 172 the landslide depth (m), and  $\varphi$  is the effective internal friction angle ( $^\circ$ ).

173 The left-hand side of Eq. (3) represents the topographic condition of a given landslide or a site susceptible to  
 174 slope failure (Montgomery et al., 2000). Moving  $R$  to the left-hand side yields the right-hand side of Eq. (4) in an  
 175 integrated form involving only soil mass parameters:

176 
$$a_{cr} \times R_t = \frac{K \tan\theta (C' + C_r)}{\rho_w g \tan\varphi} + zK\sin\theta\cos\theta \frac{\rho_s}{\rho_w} \left( 1 - \frac{\tan\theta}{\tan\varphi} \right) \quad (4)$$

177 The physical meaning of  $a_{rc} \times R_t$  is that hillslope resistance to failure under site-specific topographic conditions and  
 178 a given rainfall input strongly depends on soil physical properties. For the rain-induced loessal landslides in the  
 179 study area, the strength and hydraulic properties of the landslide mass in woodland and shrubland may lead to  
 180 different  $a_{rc} \times R_t$  levels, so that landslide density (or number) differs between woodland and shrubland. Therefore,  
 181 we focus on  $a_{rc} \times R_t$  from the right-hand side of Eq. (4) to elucidate the initiation of loessal landslides in two forested  
 182 land types.

## 183 4 Results

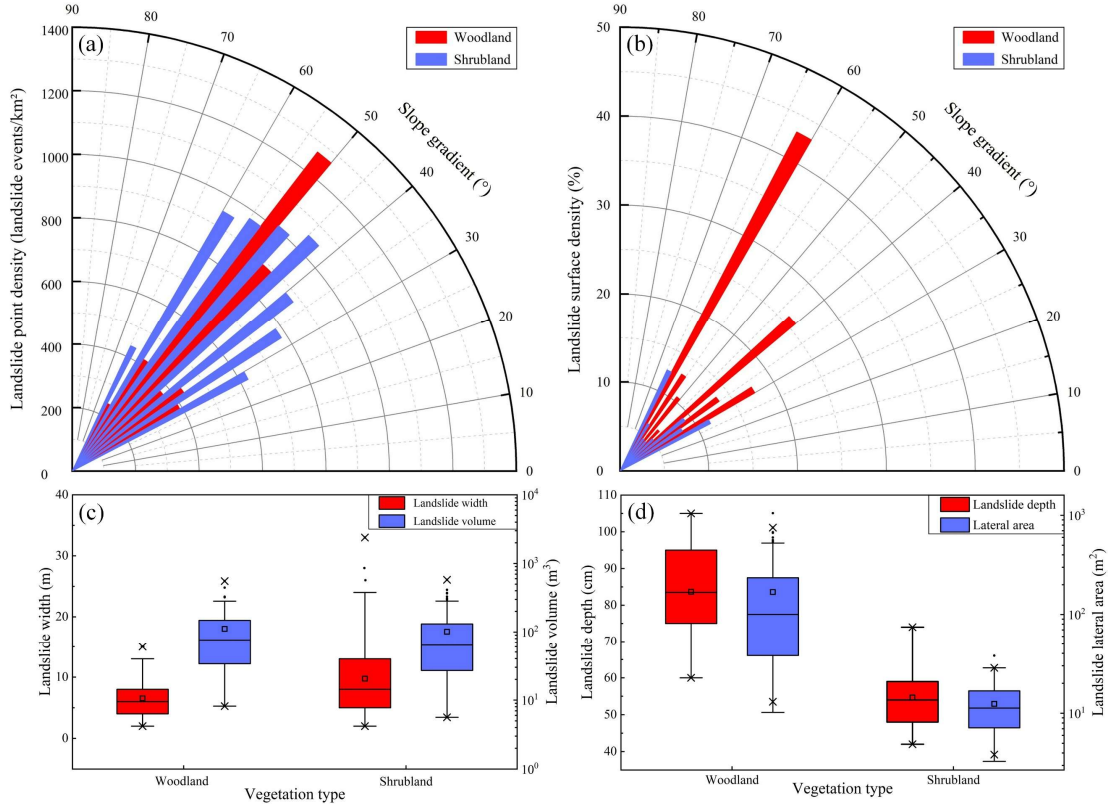
### 184 4.1 Landslides in the two lands

185 To compare the landslide point and areal densities between the two stands, we calculated landslide counts and  
 186 areas and divided them by the total steep-terrain area in each stand. This approach excluded non-susceptible terrain  
 187 from the analysis. The spatial distribution and morphology of landslides in woodland and shrubland exhibited clear  
 188 patterns. Specifically, the statistical results showed that landslide point density in shrubland was 1.56 times that in  
 189 woodland, whereas landslide areal density was only 0.48 times that in woodland (Figs. 5a and 5b). Furthermore, the  
 190 average landslide width in shrubland was 1.49 times that in woodland. Generally, trees in woodlands have deep root  
 191 systems that provide stronger anchoring and can mobilize deeper soil layers, thereby modifying the failure depth  
 192 and geometry of shallow landslides (Schwarz et al., 2010; Masi et al., 2023; Dibiagio et al., 2024). The average  
 193 landslide depth in woodland was 1.82 times that in shrubland, while the average lateral extent was 1.61 times that in  
 194 shrubland. However, the average width of landslides in woodland was only 0.67 times that in shrubland. Overall,  
 195 the total landslide volume in woodland was 1.16 times that in shrubland, indicating that landslides in woodland tend  
 196 to be larger (Figs. 5c and 5d).

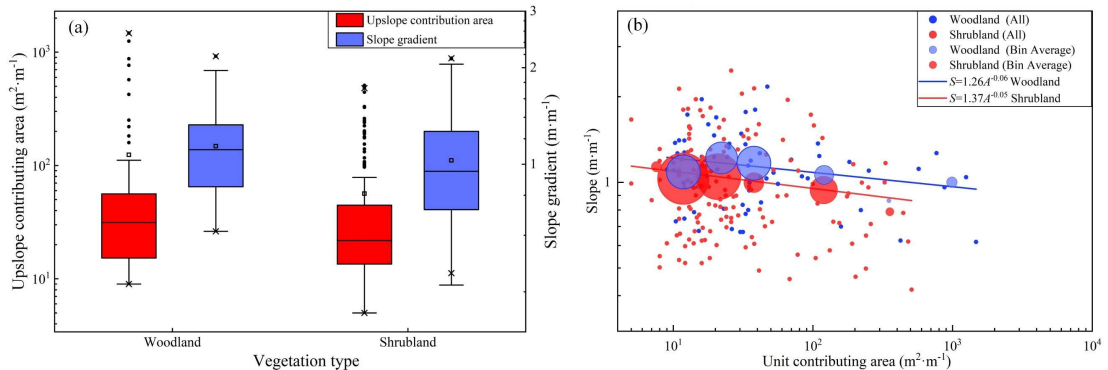
197 When landslides are considered alongside other landscape-dissection agents such as rills and gullies, their  
 198 spatial locations depend on two controls. One is spatial competition between the slope-dependent term  $S = \tan\theta$   
 199 ( $\text{m} \cdot \text{m}^{-1}$ ) and the area-dependent term  $A$  ( $\text{m}^2 \cdot \text{m}^{-1}$ ); the other is exceedance of the  $A$ - $S$  topographic threshold  
 200 (Montgomery and Dietrich, 1994). As highlighted in Sect. 3.4, variations in  $a_{rc} \times R_t$  arise from the interplay of  
 201 topography, failure depth, soil strength, plant root reinforcement, and hydraulic conductivity. To evaluate these  
 202 controls on landslides, we compared the upslope contributing area ( $A$ ) and slope gradient ( $S$ ) between the two land  
 203 types.

204 Field investigations reveal that most landslides in the study area occur in concave topographic positions.  
 205 Statistical analysis indicates that, on average, woodland sites have a significantly larger upslope contributing area  
 206 ( $124 \text{ m}^2 \text{ m}^{-1}$ ) and steeper slopes ( $48^\circ$ ) than shrubland sites. These values are consistent with expectations from the  
 207  $A$ - $S$  threshold framework (Fig. 6a). Fitting regression lines to the bin-averaged dataset further demonstrates that

208 landslides in woodland generally require either a larger upslope contributing area or a steeper slope gradient for  
 209 initiation (Fig. 6b). The  $A-S$  relationship shows that, at similar slope gradients, landslides in woodland require larger  
 210 upslope contributing areas than those in shrubland. This suggests that, compared with landslides in shrubland, those  
 211 in woodland may require higher rainfall-intensity thresholds, steeper slopes, or both, for initiation. Consistent with  
 212 this, shrubland shows a higher landslide point density than woodland (1.56 times; Fig. 5a).



213  
 214 **Figure 5.** Landslide characteristics in woodland and shrubland. (a) point density by slope-gradient class; (b) areal  
 215 density by slope-gradient class; (c) landslide width and volume; and (d) landslide depth and lateral area. The three  
 216 horizontal-lines of box show decreasing order of 75th quantile ( $Q_3$ ), median ( $Q_2$ ), and 25th quantile ( $Q_1$ ). The box  
 217 length is the interquartile range ( $IQR=Q_3-Q_1$ ). The small square is the average value. The cross symbols denote the  
 218 1st and 99th percentiles. The upper and lower limit of whiskers are  $Q_3+1.5IQR$  and  $Q_1-1.5IQR$ , respectively. The  
 219 whiskers extend to the most extreme values within these limits; mild outliers are shown as black dots.



220  
 221 **Figure 6.** Upslope contributing area and slope gradient condition. (a) upslope contributing area and mean slope as  
 222 a function of slope aspect; (b) upslope contributing area vs. mean slope gradient above the landslide area. The

223 definition of the boxplots is given in the caption of Fig. 5. Circles indicate mean slopes, with radius proportional to  
 224 the number of landslides. A power-law regression is fitted to the bin-averaged data.

## 225 4.2 Soil Hydrological properties

### 226 4.2.1 SWCC and HCF curves

227 Mean landslide depths in woodland and shrubland are 0.84 m and 0.55 m, respectively (Fig. 5d). Soil-moisture  
 228 monitoring and soil sampling were conducted at three depth intervals (0–30, 30–60, and 60–90 cm), as described in  
 229 Sect. 3.2. Because observed landslide depths in woodland were mostly within 60–90 cm, this layer was taken as the  
 230 representative sliding layer for woodland. Likewise, because observed landslide depths in shrubland were mostly  
 231 within 30–60 cm, this layer was taken as the representative sliding layer for shrubland. Loess slopes generally remain  
 232 unsaturated during natural rainfall infiltration and drainage (Lan et al., 2021; Wei et al., 2022). Therefore, we used  
 233 the SWCC and HCF to analyze unsaturated hydro-mechanical differences between sliding-layer soils in woodland  
 234 and shrubland.

235 Table 1 lists the sliding-layer soils parameters obtained through Hydrus-1D inversion. Based on these  
 236 parameters, the SWCC and HCF were plotted for the woodland and shrubland sliding-layer soils (Fig. 7). The results  
 237 indicate that the pore-size distribution parameter and saturated hydraulic conductivity are significantly higher for  
 238 woodland soils than for shrubland soils. This contrast is evident in both drying and wetting processes. This suggests  
 239 that the pore system in woodland soils is dominated by larger pores, which enhance water movement. This pore  
 240 structure facilitates rainfall infiltration into the soil. In contrast, shrubland soils contain more micropores that retain  
 241 more water. This is reflected in a 3.1% higher residual water content in shrubland soils than in woodland soils.  
 242 During the drying test, the air-entry pressures of woodland and shrubland soils are nearly identical. However, during  
 243 the wetting process, the air-entry pressure in woodland soils is 0.05 kPa lower than in shrubland soils. This indicates  
 244 that larger pores in woodland soils begin to drain and fill with air at lower matric suction. This promotes air-water  
 245 exchange and moisture release, making it less likely for the soil to reach or maintain a high degree of saturation for  
 246 extended periods. Therefore, under the same rainfall conditions, shrubland soils have weaker moisture-buffering  
 247 capacity than woodland soils, making the soil more prone to becoming highly saturated. This reduces the effective  
 248 stress and shear strength of shrubland soils, ultimately reducing slope stability.

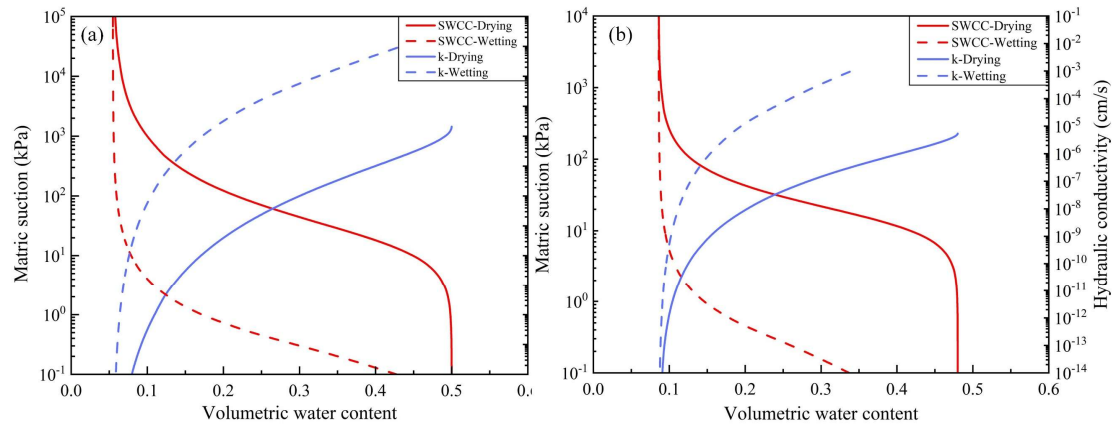
249 During the drying and wetting processes, the difference in saturated water content in shrubland sliding-layer  
 250 soil (0.101) is approximately 14.43 times that in woodland sliding-layer soil (0.007). This indicates that the pore  
 251 structure in shrubland sliding-layer soil is less stable than in woodland sliding-layer soil. Under extreme drying-  
 252 wetting conditions, some pores tend to collapse or rearrange, making it difficult for the soil to maintain its original  
 253 pore configuration. The resulting changes in pore structure disrupt water flow paths in shrubland sliding-layer soil,  
 254 reducing permeability, weakening water flow, and slowing drainage. These findings are consistent with the stronger  
 255 hysteresis observed in the SWCC of shrubland sliding-layer soil compared with that of woodland sliding-layer soil  
 256 (Figs. 7a and 7b). They further confirm that woodland sliding-layer soil has a greater capacity for moisture  
 257 redistribution.

258 **Table 1.** Parameters describing the soil water characteristic curve (SWCC) and the hydraulic conductivity function  
 259 (HCF) for the sliding-layer soils used in Hydrus 1D

Parameters	Definition	Woodland	Shrubland
$\theta_s^d$	Saturated water content	0.500	0.480
$\theta_s^w$		0.493	0.379
$\theta_r$	Residual water content	0.055	0.086
$n^d$	The pore size distribution parameter	1.58	2.19
$n^w$		1.69	1.88

$\alpha^d$ (KPa <sup>-1</sup> )		$5.461 \times 10^{-3}$	$6.294 \times 10^{-3}$
$\alpha^w$ (KPa <sup>-1</sup> )	The inverse of the air entry pressure head	0.646	0.596
$K_s^d$ (cm·s <sup>-1</sup> )		$2.3 \times 10^{-5}$	$5.4 \times 10^{-6}$
$K_s^w$ (cm·s <sup>-1</sup> )	Saturated hydraulic conductivity	$7.1 \times 10^{-2}$	$5.0 \times 10^{-3}$

260 Notes: Superscripts "d" and "w" denote the drying and wetting processes, respectively.

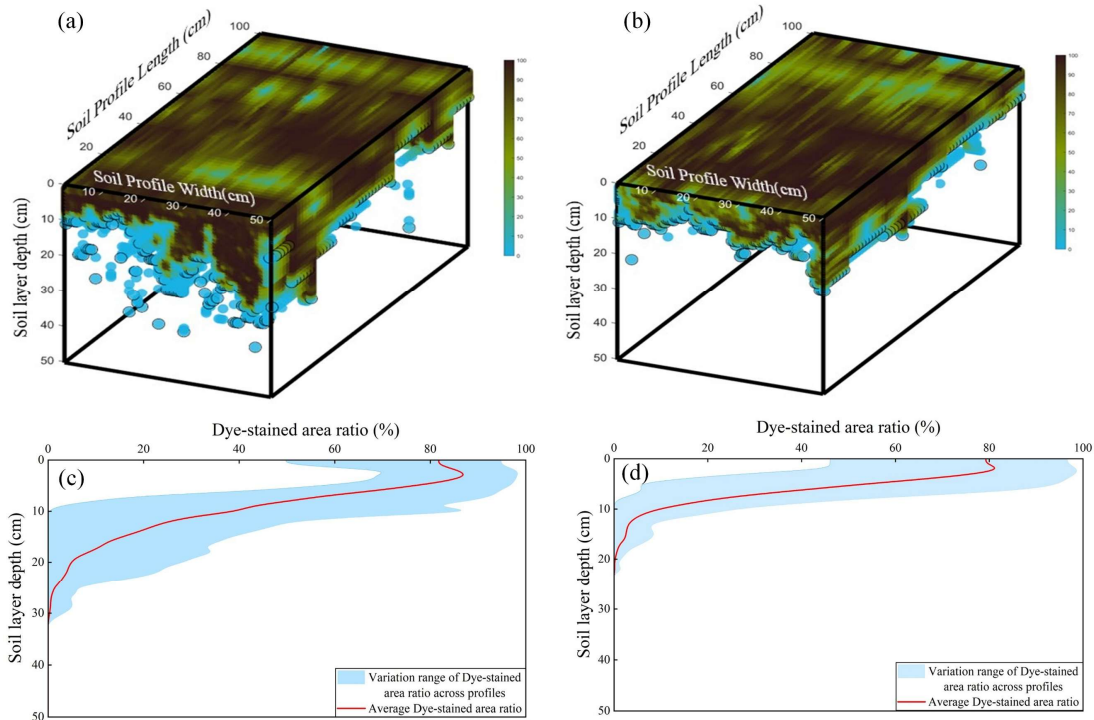


261  
262 **Figure 7.** Differences in the hydromechanical properties of the sliding-layer soils. **(a)** SWCC for layer 3 of the  
263 woodland soil profile; **(b)** SWCC for layer 2 of the shrubland soil profile.

#### 264 4.2.2 Dye tracer experiments

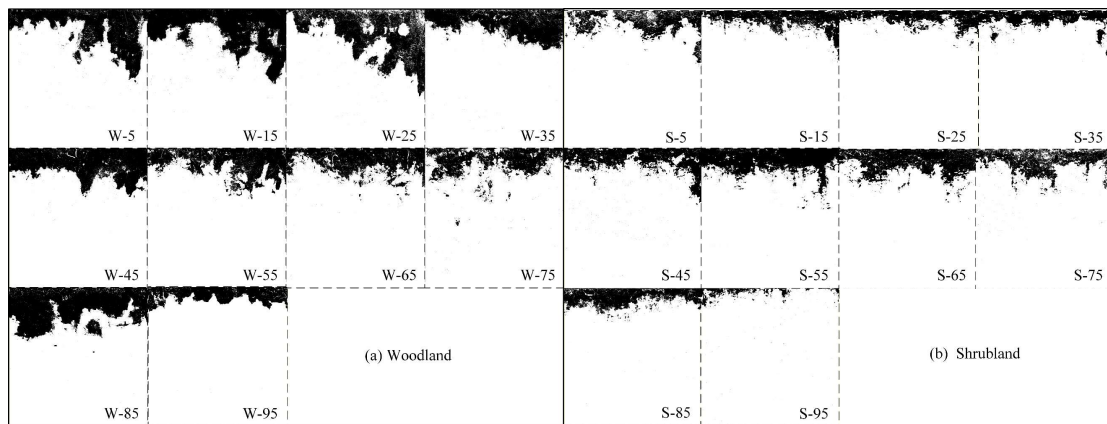
265 Dye-tracer experiments directly visualize the flow pathways of water infiltration in woodland and shrubland  
266 soils. Under the same applied water volume and infiltration area, the stained soil volume in woodland soils is  
267 markedly larger than that in shrubland soils. Three-dimensional visualizations reveal that stained pathways in  
268 woodland soils form thick bands with numerous vertically continuous columnar channels. Hydraulic connectivity is  
269 high, and water infiltrates to greater depths. Stained bands in shrubland soils are shallow, and vertical, filament-like  
270 channels are nearly absent. In addition, the depth-dependent pattern of dye-stained area ratios in the shrubland profile  
271 further confirms that vertical infiltration is restricted to relatively shallow depths. Differences in the volume, depth,  
272 and morphology of the stained pathways indicate that infiltration in woodland soils no longer follows uniform  
273 matrix-flow conditions. This is also evident in the dye-stained areas of vertical profiles. Woodland profiles show  
274 large, continuous color patches, whereas shrubland profiles mainly show fragmented spots concentrated in shallow  
275 soil. This pattern suggests that deeper shrubland soils are denser and have lower pore connectivity.

276 Overall, woodland soils more readily develop a stable, efficient vertical percolation system with greater  
277 infiltration depth and stronger connectivity. This promotes deep water storage and redistribution. In contrast,  
278 insufficient pore connectivity in shrubland soils causes water to remain in shallow layers, prolonging surface wetness  
279 and slowing pore-water pressure recovery. Under intense rainfall, this condition favors saturation buildup and thus  
280 increases the likelihood of landslide initiation. This flow pattern is consistent with the SWCC- and HCF-inferred  
281 differences in soil hydraulic behavior and provides direct, pathway-scale evidence of flow pathways, which cannot  
282 be resolved from the curve-derived hydraulic parameters alone.



283

284 **Figure 8.** Morphological characteristics of dye-stained flow paths in woodland and shrubland soils. **(a)** Three-  
 285 dimensional visualization of stained zones in woodland; **(b)** Three-dimensional visualization of stained zones in  
 286 shrubland; **(c)** Dye-stained area ratio vs. soil depth in woodland; **(d)** Dye-stained area ratio vs. soil depth in shrubland.

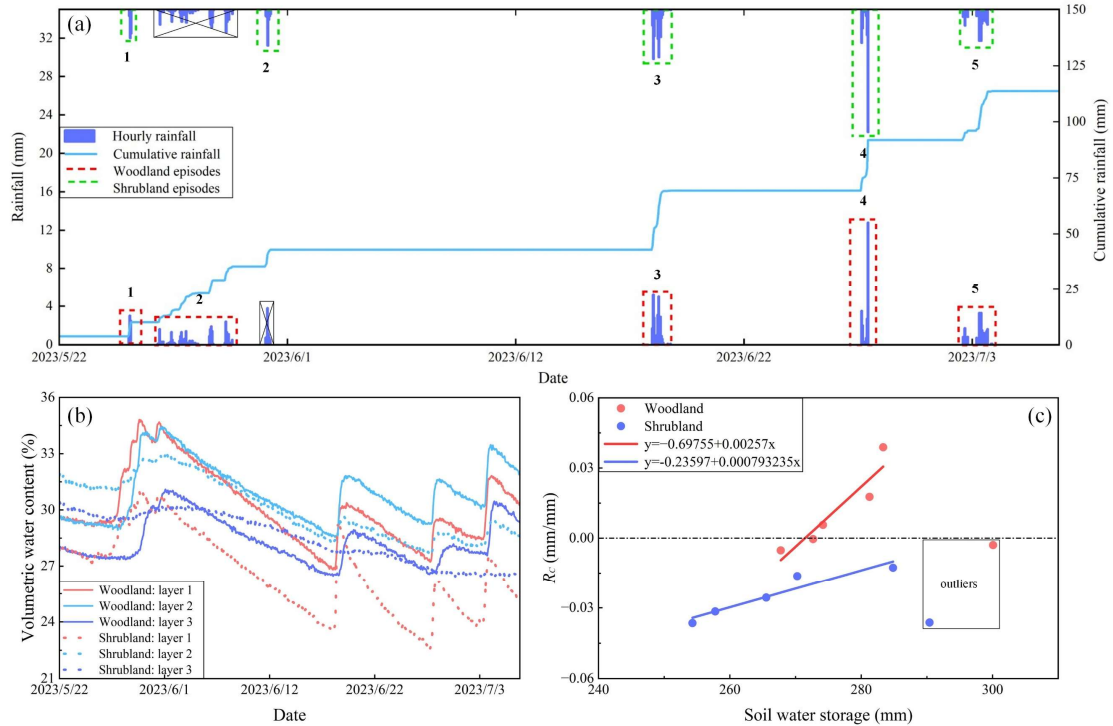


287

288 **Figure 9.** Schematic dye-stained vertical soil profiles at different hillslope positions. **(a)** Woodland profile; **(b)**  
 289 Shrubland profile. Numbers from 0 to 100 denote relative slope positions, with lower values indicating locations  
 290 near the slope base.

### 291 4.3 Slope hydrological characteristics

292 To characterize how woodland and shrubland soils respond to rainfall, we group rainfall events into distinct  
 293 episodes based on soil depth and in rain saturated hydraulic conductivity (Fig. 10a). Using these episodes as the  
 294 basic analytical units, we then assess the intensity of slope-surface responses and the associated water distribution.  
 295 This approach overcomes the limitations of using rainfall statistics alone. It explicitly addresses the slope's dynamic  
 296 absorption-response behavior and shifts the focus from single-storm triggering to a more comprehensive assessment  
 297 of cumulative rainfall-response lags.



298  
299  
300  
301

**Figure 10.** Analysis of rainfall, soil moisture, and their coupling from 22 May to 7 July 2023. **(a)** Classification of rainfall episodes by vegetation type; **(b)** Temporal variation in volumetric soil water content for woodland and shrubland; **(c)** Coupling between rainfall input and soil-moisture response for woodland and shrubland.

302  
303  
304  
305  
306  
307

From 22 May to 7 July 2023, volumetric water content indicates that shrubland soils beneath the sliding layer (layer 3) are insensitive to rainfall and show only small variations in water content (Fig. 10b). This is consistent with the findings in Sect. 4.2. In shrubland, most water remains near the surface, and infiltration capacity is low. To characterize the rainfall-soil-water coupling process, we introduce the index  $R_c$ , which quantifies how efficiently rainfall is converted into soil-water storage (Fig. 10c). A steeper slope in the regression of  $R_c$  versus soil water storage indicates a stronger soil-moisture response to rainfall.

308  
309  
310  
311  
312  
313  
314  
315  
316

In woodland,  $R_c$  values are generally positive, indicating that increases in soil-water content often exceed local rainfall input. Woodland soils have better-developed preferential flow paths than shrubland soils. This suggests that the observed excess arises because water infiltrating into upslope soils moves downslope as subsurface flow. This interpretation is consistent with the dye-tracer experiments. In woodland, foot-slope profiles show greater staining depths than upslope profiles (Fig. 8a). By contrast, early shallow saturation in shrubland diverts part of the rainfall input into overland flow, reducing conversion efficiency and yielding mostly negative  $R_c$  values. Overall, high  $R_c$  values in woodland reflect a strong hydrological response to rainfall and a greater capacity to buffer soil moisture. In shrubland, a pronounced response lag and low conversion efficiency lead to negative  $R_c$  values. These patterns are consistent with the earlier mechanism-based interpretation.

317

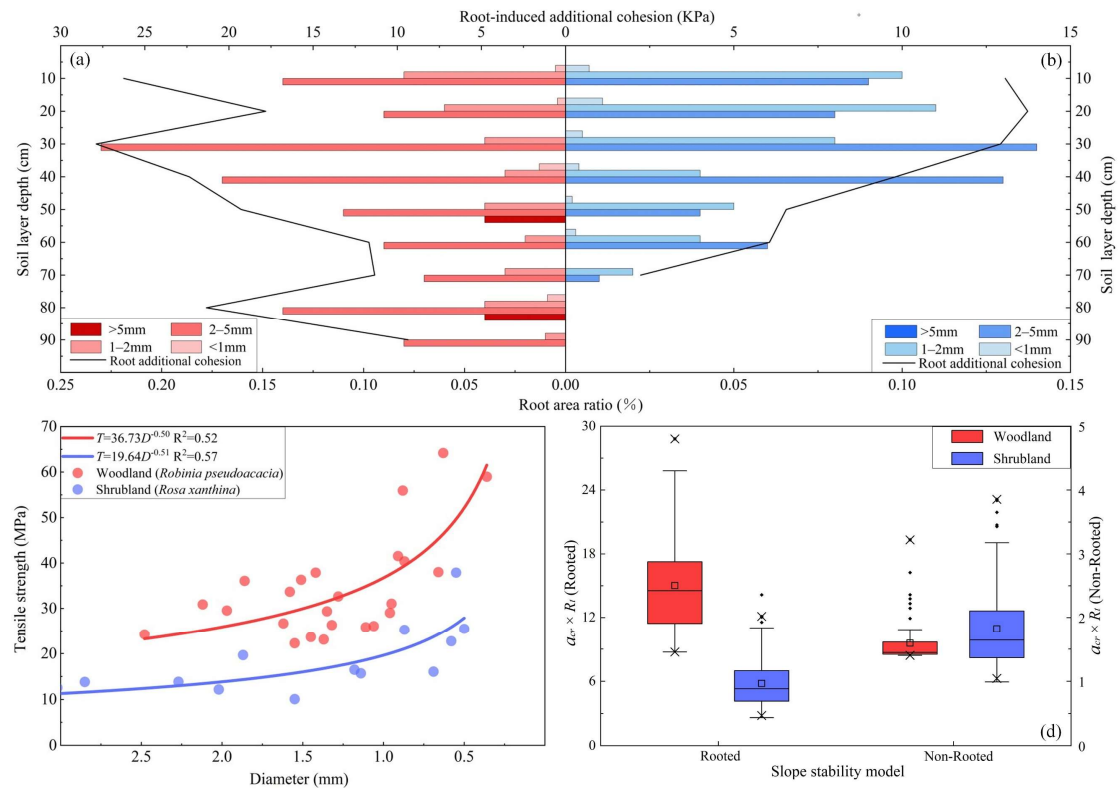
#### 4.4 Effects of vegetation roots on hillslope stability

318  
319  
320  
321  
322

Root spatial distribution and mechanical properties differ markedly between woodland and shrubland soils (Figs. 11a, 11b, and 11c). Field measurements indicate that maximum rooting depths in *Robinia pseudoacacia* and *Rosa xanthina* are close to their respective mean landslide depths, at 0.84 m in *Robinia pseudoacacia* and 0.54 m in *Rosa xanthina*. This consistency indicates a close relationship between root distribution and landslide depth. Compared with *Rosa xanthina*, roots in *Robinia pseudoacacia* mobilize greater root-induced cohesion at a given

323  
324

root diameter and exhibit a larger specific root area ratio (*RAR*). These roots therefore create a more extensive root-soil contact interface and form a mechanically stronger root-soil composite.



325  
326  
327  
328  
329

**Figure 11.** Mechanical indices of slope stability in woodland and shrubland. **(a)** Root area ratio and root-induced cohesion in woodland (*Robinia pseudoacacia*); **(b)** Root area ratio and root-induced cohesion in shrubland (*Rosa xanthina*); **(c)** Relationship between root tensile strength and diameter; **(d)** Slope-stability models for woodland and shrubland. The definitions of the boxplots is given in the caption of Fig. 5.

330  
331  
332  
333  
334  
335  
336  
337  
338

Using the parameters in Table 2, we constructed a slope stability model to evaluate slope resistance to failure under specified topographic conditions and rainfall inputs. When root-induced cohesion is ignored, mean  $a_{rc} \times R_t$  values in woodland and shrubland are similar, indicating that slope stability differs little between them. When root effects are included, slope stability increases markedly. In woodland, the  $a_{rc} \times R_t$  value rises to 15.02, approximately 338% higher than in shrubland (Fig. 11d). These results indicate that woodland roots contribute much more to slope stability than roots in shrubland. Woodland roots substantially increase the critical rainfall and topographic thresholds for landslide initiation and confirm the key role of roots in strengthening slopes and resisting landslide-triggering factors.

**Table 2** Parameters describing the slope stability model

Parameters	Definition	Woodland	Shrubland
$\rho_s$ ( $\text{kg} \cdot \text{m}^{-3}$ )	Dry soil density	1.37	1.41
$\theta$ ( $^\circ$ )	Slope gradient	31.71–65.27	22.78–67.96
$C'$ (kPa)	Effective soil cohesion	5.97	7.35
$C_r$ (kPa)	Root-induced cohesion	18.59	10.36
$\varphi$ ( $^\circ$ )	Effective friction angle	18.67	14.50
$z$ (m)	Landslide depth	0.84	0.54
$K$ ( $\text{mm} \cdot \text{h}^{-1}$ )	Hydraulic conductivity	2.10	0.94

## 339 5 Discussion

340 Long-term vegetation restoration policies may result in the dominant soil erosion process shift from traditional  
341 wind and water erosion to landslides (Deng et al., 2022; Yang et al., 2024; Du et al., 2025; Liao et al., 2025).  
342 Ecological restoration forests not only increase surface cover, but the recovered vegetation extends their root systems  
343 into potential sliding layers, thereby substantially altering slope hydrological processes and mechanical properties,  
344 and playing an important role in landslide initiation (Zhao et al., 2022; Cai et al., 2024; Chen et al., 2024; Lann et  
345 al., 2024). In this context, our results highlight the hydro-mechanical heterogeneity across the *Robinia pseudoacacia*-  
346 dominated woodland and *Rosa xanthina*-dominated shrubland, and assessed its influence on landslide initiation.

347 The results of SWCC and HCF agree well with the infiltration patterns observed in dye-tracer experiments. In  
348 woodland soils, continuous preferential flow channels promote rapid infiltration, substantial downward water  
349 migration, and a high capacity for water storage and drainage. Shrubland soils exhibit scattered preferential flow  
350 channels, shorter infiltration pathways, pronounced shallow saturation, and a weaker capacity for water  
351 redistribution. The stained area ratio and patch distribution further corroborate these differences. Woodland profiles  
352 display vertical and continuous stained bands with greater infiltration depths, whereas shrubland profiles show  
353 shallow staining. This comparison indicates that variations in root distribution and diameter modify soil pore  
354 structure and thereby affect infiltration (Guan et al., 2024; Lann et al., 2024). Woodland soil with coarse roots and  
355 higher porosity facilitate deeper infiltration, whereas shrubland soils with shallow root systems provide lower  
356 infiltration capacity (Souza et al., 2023; Xiao et al., 2024; Hu et al., 2025). Preferential flow may result in the excess  
357 soil water storage over the rainfall depth, and the results from monitoring multiple natural rainfall events between  
358 20 May and 6 July 2023 further corroborate the assumption. In shrubland, soil moisture typically exhibits a delayed  
359 and attenuated response to rainfall.  $R_C$  values are consistently below zero, indicating low rainfall conversion  
360 efficiency. Most rainwater does not infiltrate but instead runs off once shallow soils saturate rapidly. In contrast,  
361 once rainfall over woodland slopes reaches a certain intensity,  $R_C$  values become positive. This pattern suggests that  
362 woodland slopes effectively intercept and infiltrate rainfall, sustain deeper water storage, and delay the development  
363 of saturation zones. This discrepancy is also evident in the critical  $a_{rc} \times R_t$  values. The failure resistance on woodland  
364 slopes is higher than shrubland slopes, which may explain the contrasting distribution patterns observed in landslide  
365 number and size.

366 Vegetation-based slope protection has long been regarded as a key measure in traditional soil and water  
367 conservation, yet multidisciplinary studies have revealed its dual effects (Gyssels et al., 2005; Sidle and Bogaard,  
368 2016; Lann et al., 2024). Some herbaceous plants with shallow root systems can promote rapid surface saturation  
369 during intense rainfall, thereby enhancing hillslope runoff and rill erosion (Gong et al., 2024). Certain fast-growing  
370 tree species with shallow root systems may provide only limited soil reinforcement and thus increase the risk of  
371 shallow landslides (Ghestem and Sidle, 2011; Lin et al., 2024). Moreover, excessively thick litter layers can impede  
372 infiltration during short-duration storms and accelerate runoff concentration (Zhou et al., 2018; Rajão et al., 2023).  
373 These observations indicate that vegetation-based measures are not universally effective for soil erosion control  
374 (Löbmann et al., 2020; Lann et al., 2024). Our results further support this understanding. Shallow landslide initiation  
375 depends not only on rainfall but also on vegetation type, which modifies coupled hydrological-mechanical processes  
376 on slopes. The deep root systems and stable preferential flow channels in woodland slopes may provide greater  
377 resilience against slope failure compared to shrubland slopes. This finding provides empirical evidence for forest-  
378 type allocation in ecologically sensitive areas. It also highlights the need for appropriate vegetation-type selection  
379 and matching in regional soil and water conservation.

## 380 **6 Conclusions**

381 Vegetation recovery on the Chinese Loess Plateau has altered the dominant soil erosion process from runoff-  
382 driven erosion to gravity-driven mass movements. Though previous studies have extensively investigated vegetation  
383 effects on soil erosion, the specific role of vegetation in landslide initiation remains poorly understood. In this study,  
384 we systematically examined landslide initiation processes in two contrasting vegetated landscapes: *Robinia*  
385 *pseudoacacia*-dominated woodlands and *Rosa xanthina*-dominated shrublands, focusing on hydro-mechanical  
386 heterogeneity. Following results can be drawn:

387 1. Landslides in woodland and shrubland exhibit obvious differences in initiation, depth and number. Shrubland  
388 has a higher density of small, shallow landslides, whereas woodland has fewer but deeper and larger failures. This  
389 contrast reflects a high-initiation-threshold and deep-seated-failure regime in woodland.

390 2. In shrubland, a loose, discontinuous pore system and pronounced hysteresis concentrate moisture in shallow  
391 layers, causing rapid shallow saturation and large rainfall losses. In woodland, stable preferential flow paths promote  
392 deeper and more efficient moisture migration, as reflected in higher soil water response index.

393 3. Woodland roots extend deeper and span a wider depth range than shrubland roots. Within the same depth  
394 interval, root additional cohesion and *RAR* are also higher than those in shrubland. These patterns indicate stronger  
395 root-network reinforcement in woodland soils and lower susceptibility to shallow landslides than in shrubland.  
396 Therefore, the sediment production from landslide erosion may differ in various forest types, which has been rarely  
397 addressed and deserves further study in future.

## 398 **Acknowledgments**

399 This research has been supported by the State Key Program of Natural Science of China (grant no. 42130701), and  
400 the Natural Science Foundation of China (grant no. 42177309). The authors extend their gratitude to personnel at  
401 the Jixian National Ecosystem Research Station of Shanxi Province, Beijing Forestry University, for their help during  
402 field investigations.

## 403 **Code and data availability**

404 The corresponding author, Prof. Chao Ma, is willing to share the raw/processed data upon reasonable request.

## 405 **Author contributions**

406 **Prof. Ma** conceived the study based on his expertise in shallow landslides and unsaturated soil mechanics, and  
407 proposed the concept of hydrological and hydromechanical coupling for analyzing vegetation-related slope  
408 instability. Under the guidance of Prof. Ma, **Ruijie Yang** conducted soil hydrology experiments and drafted the  
409 manuscript. **Xi Yang and Xinying Wang** assisted with field investigations. **Yan Zang and Liqun Lyu** contributed  
410 research progress on shallow landslides and vegetation–slope interactions in the study area.

## 411 **Competing interests**

412 The authors declare no conflicts of interest.

## 413 **References**

- 414 An, J., Gao, G., Yuan, C., and Fu, B.: Inter- and intra-event rainfall partitioning dynamics of two typical xerophytic  
415 shrubs in the loess plateau of china, *Hydrology and Earth System Sciences Discussions*, 26, 3885-3900,  
416 <https://doi.org/10.5194/hess-26-3885-2022>, 2022.  
417 Bachmair, S., Weiler, M., and Troch, P. A.: Intercomparing hillslope hydrological dynamics: spatio-temporal

418 variability and vegetation cover effects, *Water Resour. Res.*, 48, W5537, <https://doi.org/10.1029/2011WR011196>,  
419 2012.

420 Bai, R., Wang, X., Li, J., Yang, F., Shangguan, Z., and Deng, L.: The impact of vegetation reconstruction on soil  
421 erosion in the loess plateau, *J. Environ. Manage.*, 363, 121382, <https://doi.org/10.1016/j.jenvman.2024.121382>,  
422 2024.

423 Borrelli, P., Robinson, D. A., Panagos, P., Lugato, E., Yang, J. E., Alewell, C., Wuepper, D., Montanarella, L., and  
424 Ballabio, C.: Land use and climate change impacts on global soil erosion by water (2015-2070), *Proc. Natl. Acad.  
425 Sci. U. S. A.*, 117, 21994-22001, <https://doi.org/10.1073/pnas.2001403117>, 2020.

426 Cai, L., Wang, F., Lin, Y., Long, Q., Zhao, Y., Han, J., Ge, W., and Chen, H.: Changes in preferential flow caused  
427 by root effects in black locust plantations of different stand ages in the semi-arid region of the loess plateau, *J.  
428 Hydrol.*, 634, 131086, <https://doi.org/10.1016/j.jhydrol.2024.131086>, 2024.

429 Chen, M., Yang, X., Zhang, X., Bai, Y., Shao, M., Wei, X., Jia, Y., Wang, Y., Jia, X., Zhu, Y., Zhang, Q., Zhu, X.,  
430 and Li, T.: Response of soil water to long-term revegetation, topography, and precipitation on the chinese loess  
431 plateau, *Catena*, 236, 107711, <https://doi.org/10.1016/j.catena.2023.107711>, 2024.

432 Deng, J., Ma, C., and Zhang, Y.: Shallow landslide characteristics and its response to vegetation by example of july  
433 2013, extreme rainstorm, central loess plateau, china, *Bull. Eng. Geol. Environ.*, 81, 100, [https://doi.org/10.1007/  
434 s10064-022-02606-1](https://doi.org/10.1007/s10064-022-02606-1), 2022.

435 Dibiagio, A., Capobianco, V., Oen, A., and Tallaksen, L. M.: State-of-the-art: parametrization of hydrological and  
436 mechanical reinforcement effects of vegetation in slope stability models for shallow landslides, *Landslides*, 21,  
437 2417-2446, <https://doi.org/10.1007/s10346-024-02300-1>, 2024.

438 Du, P., Chen, Y., Zhao, Y., Qu, L., Liu, H., Liu, Z., Xu, J., and Tian, X.: Formation process and depositional  
439 characteristics of mudballs in the loess plateau during extreme rainstorms: dual-threshold constraints on material  
440 sources and dynamic conditions, *J. Environ. Manage.*, 391, 126590, [https://doi.org/10.1016/j.jenvman.2025.  
441 126590](https://doi.org/10.1016/j.jenvman.2025.126590), 2025.

442 Fan, L., Lehmann, P., Zheng, C., and Or, D.: Rainfall intensity temporal patterns affect shallow landslide triggering  
443 and hazard evolution, *Geophys. Res. Lett.*, 47, e2019GL085994, [https://doi.org/https://doi.org/10.1029/2019GL  
444 085994](https://doi.org/https://doi.org/10.1029/2019GL085994), 2020.

445 Feng, X., Fu, B., Piao, S., Wang, S., Ciais, P., Zeng, Z., Lü, Y., Zeng, Y., Li, Y., Jiang, X., and Wu, B.: Revegetation  
446 in china's loess plateau is approaching sustainable water resource limits, *Nat. Clim. Chang.*, 6, 1019-1022,  
447 <https://doi.org/10.1038/nclimate3092>, 2016.

448 Franklin, S. M., Kravchenko, A. N., Vargas, R., Vasilas, B., Fuhrmann, J. J., and Jin, Y.: The unexplored role of  
449 preferential flow in soil carbon dynamics, *Soil Biology and Biochemistry*, 161, 108398, [https://doi.org/10.1016/  
450 j.soilbio.2021.108398](https://doi.org/10.1016/j.soilbio.2021.108398), 2021.

451 Fu, B., Wang, S., Liu, Y., Liu, J., Liang, W., and Miao, C.: Hydrogeomorphic ecosystem responses to natural and  
452 anthropogenic changes in the loess plateau of china, *Annual Review of Earth & Planetary Sciences*, 45, 223-243,  
453 <https://doi.org/10.1146/annurev-earth-063016-020552>, 2016.

454 Ghestem, M. and Sidle, R.: The influence of plant root systems on subsurface flow: implications for slope stability,  
455 *Bioscience*, 61, 869-879, <https://doi.org/10.1525/bio.2011.61.11.6>, 2011.

456 Gong, C., Ni, D., Liu, Y., Li, Y., Huang, Q., Tian, Y., and Zhang, H.: Herbaceous vegetation in slope stabilization:  
457 a comparative review of mechanisms, advantages, and practical applications, *Sustainability*, 16, 7620,  
458 <https://doi.org/10.3390/su16177620>, 2024.

459 Gu, C., Mu, X., Gao, P., Zhao, G., Sun, W., Tatarko, J., and Tan, X.: Influence of vegetation restoration on soil  
460 physical properties in the loess plateau, china, *J. Soils Sediments*, 19, 716-728, <https://doi.org/10.1007/s11368->

461 018-2083-3, 2019.

462 Guan, N., Bi, H., Song, Y., Lu, S., Lin, D., and Han, J.: Vegetation restoration is affecting the characteristics and  
463 patterns of infiltration in the loess plateau, *Catena*, 243, 108190, <https://doi.org/10.1016/j.catena.2024.108190>,  
464 2024.

465 Gyssels, G., Poesen, J., Bochet, E., and Li, Y.: Impact of plant roots on the resistance of soils to erosion by water: a  
466 review, *Progress in Physical Geography*, 29, 189-217, <https://doi.org/10.1191/0309133305pp443ra>, 2005.

467 Hao, M., Jin, Z., Luo, D., Cao, G., Jiang, C., Han, H., Yang, S., and Zhang, J.: Rainstorm erosion difference and  
468 topographical changes induced by heavy rainfall between afforestation and grassland restoration catchments on  
469 the chinese loess plateau, *Geomorphology*, 457, 109243, <https://doi.org/10.1016/j.geomorph.2024.109243>, 2024.

470 Hu, J., Ren, Y., Tang, M., Zhang, Z., Yang, K., Zhen, Q., and Han, F.: Effects of vegetation restoration on infiltration  
471 patterns and preferential flow in semi-arid areas with shallowly buried soft bedrock (pisha sandstone) in china, *J.*  
472 *Hydrol.*, 661, 133546, <https://doi.org/10.1016/j.jhydrol.2025.133546>, 2025.

473 Lan, H., Zhao, X., Macciotta, R., Peng, J., Li, L., Wu, Y., Zhu, Y., Liu, X., Zhang, N., and Liu, S.: The cyclic  
474 expansion and contraction characteristics of a loess slope and implications for slope stability., *Sci. Rep.*, 11, 2250,  
475 <https://doi.org/10.1038/s41598-021-81821-4>, 2021.

476 Lann, T., Bao, H., Lan, H., Zheng, H., Yan, C., and Peng, J.: Hydro-mechanical effects of vegetation on slope  
477 stability: a review, *Sci. Total Environ.*, 926, 171691, <https://doi.org/10.1016/j.scitotenv.2024.171691>, 2024.

478 Laycock, W. A., Geological Survey U. S., I. B., New, J. D. O. W., United, S. F. S., and Rutgers, U. (Eds):  
479 Distribution of roots and rhizomes in different soil types in the pine barrens of new jersey, U.S. Geological Survey  
480 Professional Paper, Washington, 1967.

481 Li, F., Song, X., Tang, C., Liu, C., Yu, J., and Zhang, W.: Tracing infiltration and recharge using stable isotope in  
482 taihang mt., North china, *Environmental Geology*, 53, 687-696, <https://doi.org/10.1007/s00254-007-0683-0>, 2007.

483 Li, J., Cui, P., and Yin, Y.: Field observation and micro-mechanism of roots-induced preferential flow by infiltration  
484 experiment and phase-field method, *J. Hydrol.*, 623, 129756, <https://doi.org/10.1016/j.jhydrol.2023.129756>, 2023.

485 Li, S., Zheng, C., Lu, T., Zhou, K., Gu, Y., Wang, B., and Lu, Y.: Characteristics and influencing factors of loess  
486 terraces' preferential flow under different typical vegetation cover, *Plant Soil*, in press, <https://doi.org/10.1007/s11104-025-07710-1>, 2025.

487

488 Liang, H., Li, Y., An, X., Liu, J., Pan, N., and Li, Z.: Soil moisture dynamics and its temporal stability under  
489 different-aged caragana korshinskii shrubs in the loess hilly region of china, *Water*, 15, 2334, <https://doi.org/10.3390/w15132334>, 2023.

490

491 Liao, J., Wang, J., Jiao, J., Yan, Z., Li, J., Zhang, Z., Li, M., Xu, Q., Jiang, X., Zhao, W., Ling, Q., Sheng, H., Chen,  
492 Y., and Wu, T.: Rusle tends to overestimate soil erosion in revegetated conditions: evidence from long-term runoff  
493 plots monitoring on china's loess plateau, *Catena*, 258, 109285, <https://doi.org/10.1016/j.catena.2025.109285>,  
494 2025.

495

496 Lin, Y., Jian, W., Wu, Y., Zhu, Z., Wang, H., Dou, H., and Lai, Z.: Effect of tree roots on heavy rainfall-induced  
497 shallow landslides, *Geomatics, Natural Hazards and Risk*, 15, 2360002, <https://doi.org/10.1080/19475705.2024.2360002>, 2024.

498

499 Liu, X., Feng, T., Zhang, Y., Liu, Y., and Wang, P.: Vegetation restoration affects soil hydrological processes in  
500 typical natural and planted forests on the loess plateau, *J. Hydrol.*, 650, 132465, <https://doi.org/10.1016/j.jhydrol.2024.132465>, 2025.

501

502 Löbmann, M. T., Geitner, C., Wellstein, C., and Zerbe, S.: The influence of herbaceous vegetation on slope stability  
503 – a review, *Earth-Sci. Rev.*, 209, 103328, <https://doi.org/10.1016/j.earscirev.2020.103328>, 2020.

503 Lu, N. and Godt, J. W. (Eds): Hillslope hydrology and stability, Cambridge University Press, Cambridge, U.K.,

2013.

Lu, N., Calderon, A. R. A., Wayllace, A., Lovekin, J., and Crandall, A.: Suction stress–based rainfall intensity–duration method for slope instability prediction, *J. Geotech. Geoenviron. Eng.*, 150, 4024069, <https://doi.org/10.1061/JGGEFK.GTENG-12597>, 2024.

Masi, E. B., Tofani, V., Rossi, G., Cuomo, S., Wu, W., Salciarini, D., Caporali, E., and Catani, F.: Effects of roots cohesion on regional distributed slope stability modelling, *Catena*, 222, 106853, <https://doi.org/10.1016/j.catena.2022.106853>, 2023.

Montgomery, D. R. and Dietrich, W. E.: A physically based model for the topographic control on shallow landsliding, *Water Resour. Res.*, 30, 1153-1171, <https://doi.org/10.1029/93WR02979>, 1994.

Montgomery, D. R. and Dietrich, W. E.: Landscape dissection and drainage area-slope thresholds, in: *Process Models and Theoretical Geomorphology*, edited, John Wiley & Sons, Chichester, 221-246, 1994.

Montgomery, D. R., Schmidt, K. M., Greenberg, H. M., and Dietrich, W. E.: Forest clearing and regional landsliding, *Geology*, 28, 311-314, [https://doi.org/10.1130/0091-7613\(2000\)28<311:FCARL>2.0.CO;2](https://doi.org/10.1130/0091-7613(2000)28<311:FCARL>2.0.CO;2), 2000.

Nimmo, J. R., Perkins, K. S., Schmidt, K. M., Miller, D. M., Stock, J. D., and Singha, K.: Hydrologic characterization of desert soils with varying degrees of pedogenesis: 1. Field experiments evaluating plant-relevant soil water behavior, *Vadose Zone J.*, 8, 480-495, <https://doi.org/10.2136/vzj2008.0052>, 2009.

Niu, F., Pan, C., and Cui, Y.: Experimental investigation to the effect of different land-use on rainfall infiltration runoff patterns and preferential flow distribution in the loess area of western shanxi province, *Acta Ecologica Sinica*, 43, 4144-4166, <https://doi.org/10.5846/stxb202204130989>, 2023.

Rajão, P., Berg, M., Cornelissen, J., and Dias, A.: The effects of leaf traits on litter rainfall interception with consequences for runoff and soil conservation, *J. Ecol.*, 111, 2662-2675, <https://doi.org/10.1111/1365-2745.14203>, 2023.

Schwarz, M., Preti, F., Giadrossich, F., Lehmann, P., and Or, D.: Quantifying the role of vegetation in slope stability: a case study in tuscany (italy), *Ecol. Eng.*, 36, 285-291, <https://doi.org/10.1016/j.ecoleng.2009.06.014>, 2010.

Sidle, R. C. and Bogaard, T. A.: Dynamic earth system and ecological controls of rainfall-initiated landslides, *Earth-Sci. Rev.*, 159, 275-291, <https://doi.org/10.1016/j.earscirev.2016.05.013>, 2016.

Souza, L. F. T., Hirmas, D. R., Sullivan, P. L., Reuman, D. C., Kirk, M. F., Li, L., Ajami, H., Wen, H., Sarto, M. V. M., Loecke, T. D., Rudick, A. K., Rice, C. W., and Billings, S. A.: Root distributions, precipitation, and soil structure converge to govern soil organic carbon depth distributions, *Geoderma*, 437, 116569, <https://doi.org/10.1016/j.geoderma.2023.116569>, 2023.

Tang, B., Jiao, J., Zhang, Y., Chen, Y., Wang, N., and Bai, L.: The magnitude of soil erosion on hillslopes with different land use patterns under an extreme rainstorm on the northern loess plateau, china, *Soil and Tillage Research*, 204, 104716, <https://doi.org/10.1016/j.still.2020.104716>, 2020.

Tang, P., Zhang, J., Li, Y., Wei, G., Hu, Y., and Zhao, J.: Effects of extreme rainfall on the morphological characteristics and spatial distribution of shallow landslides under different land use patterns in the loess region of western shanxi province, northern china, *Journal of Beijing Forestry University*, 45, 109-117, <https://doi.org/10.12171/j.1000-1522.20230070>, 2023.

Wang, N. and Zhang, T.: Soil pore structure and its research methods: a review, *Soil Water Res.*, 19, 1-24, <https://doi.org/10.17221/64/2023-SWR>, 2024.

Wang, R., Dong, Z., Zhou, Z., Wang, N., Xue, Z., and Cao, L.: Effect of vegetation patchiness on the subsurface water distribution in abandoned farmland of the loess plateau, china, *Sci. Total Environ.*, 746, 141416, <https://doi.org/10.1016/j.scitotenv.2020.141416>, 2020.

Wang, R., Dong, Z., Zhou, Z., and Wang, P.: Temporal variation in preferential water flow during natural vegetation

547 restoration on abandoned farmland in the loess plateau of china, *Land*, 8, 186, [https://doi.org/](https://doi.org/10.3390/land8120186)  
548 10.3390/land8120186, 2019.

549 Wang, X., Ma, C., Lyu, L., and Zhang, Y.: Erosion characteristics of shallow landslides under various land-use  
550 conditions: an example of the caijiachuan landslide, *Arid Zone Research*, 41, 697-705,  
551 <https://doi.org/10.13866/j.azr.2024.04.15>, 2024.

552 Wang, Y., Dong, G., Qu, L., Wu, Z., Zhao, F., and Shao, C.: Ecosystem functioning of the loess plateau in china  
553 from vegetation restoration relied largely on climate, *Forests*, 14, 27, <https://doi.org/10.3390/f14010027>, 2022.

554 Wei, Y. Z., Yao, Z. H., Chong, X. L., Zhang, J. H., and Zhang, J.: Microstructure of unsaturated loess and its  
555 influence on strength characteristics, *Sci. Rep.*, 12, 1502, <https://doi.org/10.1038/s41598-022-05464-9>, 2022.

556 Wen, S., Shao, M., and Wang, J.: Earthworm burrowing activity and its effects on soil hydraulic properties under  
557 different soil moisture conditions from the loess plateau, china, *Sustainability*, 12, 9303, [https://doi.org/](https://doi.org/10.3390/su12219303)  
558 10.3390/su12219303, 2020.

559 Xiao, T., Li, P., Fei, W., and Wang, J.: Effects of vegetation roots on the structure and hydraulic properties of soils:  
560 a perspective review, *Sci. Total Environ.*, 906, 167524, <https://doi.org/10.1016/j.scitotenv.2023.167524>, 2024.

561 Yamase, K., Ikeno, H., Hotta, N., Imawaka, M., Ohashi, M., Tanikawa, T., Todo, C., Dannoura, M., and Hirano, Y.:  
562 Effect of sprouting and corresponding root distribution of the shrub species *eurya japonica* on slope stability,  
563 *Catena*, 238, 107869, <https://doi.org/10.1016/j.catena.2024.107869>, 2024.

564 Yan, X., Nunes, J. P., Sun, J., Tang, D., Wen, Y., and Li, Z.: Restored vegetation dominates the decrease in surface  
565 and subsurface runoff on the loess plateau, *J. Hydrol.*, 640, 131730, <https://doi.org/10.1016/j.jhydrol.2024.131730>,  
566 2024.

567 Yang, B., Jiao, J., Ma, X., Zhao, W., Ling, Q., Zhang, X., Han, J., Du, P., Chen, Y., and Chen, H.: Distribution and  
568 formation of soil balls under heavy rainstorm conditions in the northern loess plateau, *J. Hydrol.*, 625, 130103,  
569 <https://doi.org/10.1016/j.jhydrol.2023.130103>, 2023.

570 Yang, B., Ma, X., Jiao, J., Zhao, W., Ling, Q., Li, J., and Zhang, X.: Magnitude and hotspots of soil erosion types  
571 during heavy rainstorm events on the loess plateau: implications for watershed management, *Catena*, 246, 108365,  
572 <https://doi.org/10.1016/j.catena.2024.108365>, 2024.

573 Zhang, S., Liu, Y., Yang, M., Tian, P., Mu, X., and Zhao, G.: Impact of vegetation restoration on preferential flow  
574 and soil infiltration capacity in the hilly region of the loess plateau, *Journal of Hydrology: Regional Studies*, 59,  
575 102333, <https://doi.org/10.1016/j.ejrh.2025.102333>, 2025.

576 Zhang, Y., Tang, Z., Zhang, J., Zhang, Z., and Zhang, M.: Visualizing preferential flow paths using dye tracer and  
577 species diversity theory methods to explore their correlation to soil properties with random forest algorithm, *J.*  
578 *Hydrol.*, 638, 131570, <https://doi.org/10.1016/j.jhydrol.2024.131570>, 2024.

579 Zhao, M., Li, D., Huang, Y., Deng, Y., Yang, G., Lei, T., and Huang, Y.: Soil matrix infiltration characteristics in  
580 differently aged eucalyptus plantations in a southern subtropical area in china, *Catena*, 217, 106490,  
581 <https://doi.org/10.1016/j.catena.2022.106490>, 2022.

582 Zhou, Q., Zhou, X., Luo, Y., and Cai, M.: The effects of litter layer and topsoil on surface runoff during simulated  
583 rainfall in guizhou province, china: a plot scale case study, *Water*, 10, 915, <https://doi.org/10.3390/w10070915>,  
584 2018.

585